

A MEMS-based Foveating LIDAR to enable Real-time Adaptive Depth Sensing

Francesco Pittaluga ^{*1} Zaid Tasneem ^{*3} Justin Folden ^{*3}
Brevin Tilmon ³ Ayan Chakrabarti ² Sanjeev J. Koppal ³

¹ NEC Labs America ² Washington University in St. Louis
³ University of Florida

Abstract. Most active depth sensors sample their visual field using a fixed pattern, decided by accuracy, speed and cost trade-offs, rather than scene content. However, a number of recent works have demonstrated that adapting measurement patterns to scene content can offer significantly better trade-offs. We propose a hardware LIDAR design that allows flexible real-time measurements according to dynamically specified measurement patterns. Our flexible depth sensor design consists of a controllable scanning LIDAR that can *foveate*, or increase resolution in regions of interest, and that can fully leverage the power of adaptive depth sensing. We describe our optical setup and calibration, which enables fast sparse depth measurements using a scanning MEMS (micro-electro mechanical) mirror. We validate the efficacy of our prototype LIDAR design by testing on over 75 static and dynamic scenes spanning a range of environments. We also show CNN-based depth-map completion of sparse measurements obtained by our sensor. Our experiments show that our sensor can realize adaptive depth sensing systems.

Keywords: LIDAR, Novel sensor, Adaptive

1 Introduction

Active depth sensors and deep networks make a potent combination that has impacted many fields, from video gaming to autonomous cars. With such deployment, vision researchers have started focusing on algorithms that close the loop between active sensing and inference—with methods for correcting deficiencies in incomplete and imperfect depth measurements[41,45], as well as those that help the system decide where to sense next [24,3].

However, such work is predicated on LiDAR systems that are flexible in the kind of measurements they make. But the capability to make such measurements does not exist in most existing LiDAR hardware, where sampling is done in a set of fixed angles, usually modulated by mechanical motors which do not allow fast changes in sensing direction without unacceptable wear-and-tear.

* Equal Contribution

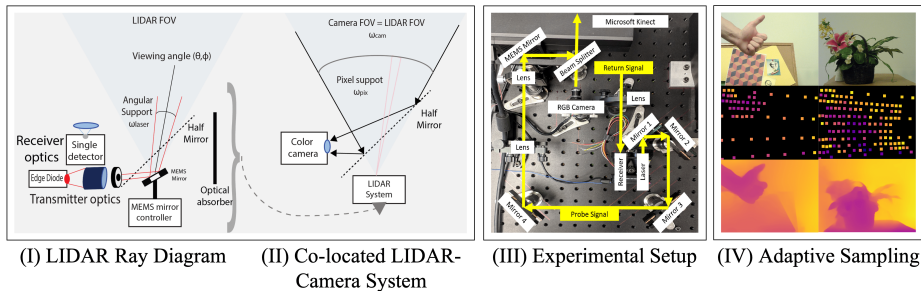


Fig. 1. ADAPTIVE LIDAR DESIGN: We have designed a flexible MEMS mirror-modulated scanning LIDAR, as shown in (I). In (II), we co-locate this directionally controllable LIDAR with a color camera, allowing for deep depth completion of the sparse LIDAR measurements. In (III) we show a picture of the hardware setup corresponding to (I-II). The long optical path is simply an artifact of having a single circuit board for both the LIDAR receiver and transmitter. In (IV) we show depth measurement for two different scenes captured with our LIDAR Prototype: color images of the scenes captured by the co-located color camera are shown in the top row, depth measurements captured by the LIDAR are shown in the middle row (note the scene-dependent scan pattern), and the corresponding outputs from our deep depth completion network are shown in the bottom row.

We present a practical, flexible, directionally controllable LiDAR platform that can leverage modern vision algorithms. It permits making measurements with different sampling patterns—providing a speed advantage when fewer measurements are made—and is co-located with a color camera to fully realize the benefits of data-driven approaches for depth completion and guided sampling.

The LIDAR’s flexibility is due to a scanning MEMS mirror, which is more compact and faster than mechanical motors. Further, the MEMS mirror is neither limited to coherent illumination, like phase arrays, nor constrained to specific light wavelengths, like photonics-based systems. We discuss the sensor design novelty, particularly the receiver optics, in comparison to other work.

To demonstrate depth sensing flexibility, we first train a deep neural network for depth completion and show that it delivers high fidelity estimates of scene geometry with our system. We evaluate this with sampling patterns of different density, that are uniform over the field of view as well as those that are concentrated in a region of interest. Finally, we show vision-driven applications to control the sensing pattern.

2 Related Work

Common depth modalities: A variety of high-quality depth sensors exist today. In Table 1 and Fig. 2 we show qualitative comparisons of our MEMS-modulated LIDAR with other sensors. Only our design demonstrates adaptive sampling, outdoors as well as indoors, even for textureless, dynamic scenes.

Sensor	Technology	Outdoors	Textureless	Adaptive
ELP-960P2CAM	Conventional Passive Stereo	✓	×	×
Kinect v1	Structured Light Stereo (LED)	×	✓	×
Kinect v2	Time-of-Flight (LED)	×	✓	×
Velodyne HDL-32E	Time-of-Flight (Laser)	✓	✓	×
Resonance MEMS	Time-of-Flight (Laser)	✓	✓	×
Our Adaptive MEMS	Time-of-Flight (Laser)	✓	✓	✓

Table 1. OUR ADAPTIVE LIDAR VS. OTHER COMMON MODALITIES: In this table we compare common depth modalities such as stereo [26], Kinect [33], Velodyne [13] and Resonance MEMS [11,39,22]. Only our LIDAR is capable of adaptive sensing, even for textureless scenes and outdoor environments.

MEMS/Galvo mirrors for vision and graphics: MEMS mirror modulation has been used for structured light [35], displays [19] and sensing [32]. In contrast to these methods, we propose to use angular control to increase sampling in regions of interest. While MEMS mirrors have been used in scanning LIDARs, such as from NASA and ARL [11,39,22], these are run at resonance, while we control the MEMS scan pattern. Such MEMS control has been shown [20] for highly reflective fiducials in both fast 3D tracking and VR applications [29,28], whereas we show results on real scenes. [37,6] show a mirror modulated 3D sensor with the potential for flexibility, but without leveraging guided networks, and we discuss the advantages of our novel receiver optics compared to these types of methods. Galvo mirrors are used with active illumination for light-transport [15] and seeing around corners [34]. Recently these have been used in light curtains for flexible, structured light reconstruction [2,43]. In contrast, ours is a MEMS-mirror driven LIDAR system with an additional capability of increasing resolution in some region of interest (i.e. zoom). In this sense, we are most related to adaptive control work [4,40,6], whereas we show both optical innovations and deep depth completion.

Adaptive Scanning Lidars: Commercially systems from AEye and Robosense are designed¹ to improve lidar-rgb fusion by adaptively changing the scanning pattern to get higher lidar resolution in regions of interest. Our focus is on compact designs for small autonomous systems and our optical innovations match that goal. [44] propose a progressive pedestrian scanning method using an actively scanned LIDAR, but results are shown in simulation rather than on a hardware platform. [40] propose directionally controlling the LIDAR scan, but these adaptive results have been shown only for static scenes. Our goal is a fast, flexible and programmable adaptive LIDAR that for real-world dynamic scenes.

Guided and Unguided Depth Completion: The impact of deep networks on upsampling and superresolution has been shown on images, disparity/depth maps, active sensor data etc. [9,27,25,41,36,18] with a benchmark on the KITTI depth completion dataset [41]. Upgrading from sparse depth samples has been

¹ The authors could not find peer-reviewed publications to verify the commercial claims.

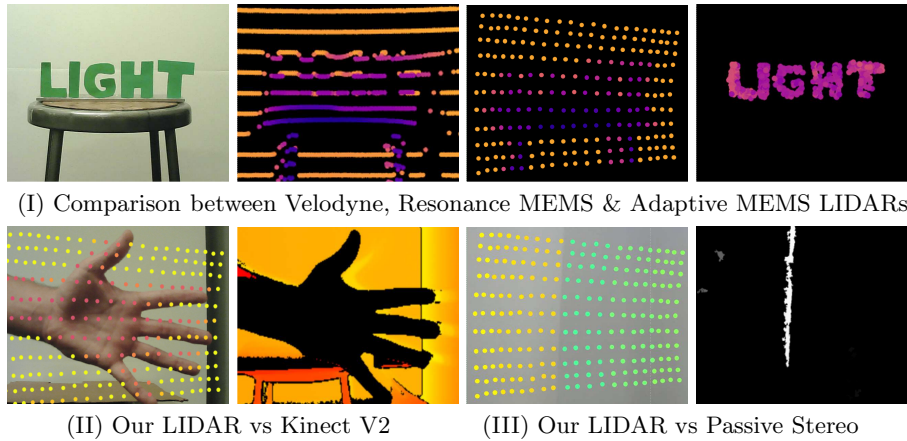


Fig. 2. QUALITATIVE COMPARISONS TO COMMON SENSORS: In (I) we compare depth measurements from our Adaptive LIDAR following a user-defined scan pattern (right), a MEMS resonance LIDAR with a uniform scan pattern [11,39,22] (middle-right), and a Velodyne HDL-32E LIDAR with uniform mechanical motion [13] (middle-left). Our adaptive LIDAR enables us to clearly resolve the individual letters. In (II) we show our LIDAR system can perform better at close-range, compared to continuous wave Kinect TOF. In (III) we compare to a working stereo sensor that only produces sparse measurements when the scene is textureless.

shown, [42], although not on a low-power platform. In addition guided upsampling has been used as a proxy for sensor fusion such as recently done for single-photon imagers [23] and flash lidar [12]. In contrast, we measure sparse low-power LIDAR depth measurements and we seek to flexibly change the sensor capture characteristics in order leverage adaptive neural networks such as [24,3].

3 Sensor design

Fig. 1 shows our sensor design, which consists of a small aperture, large depth-of-field color camera, optically co-located with a MEMS-modulated LIDAR sensor. If the camera has a FOV of ω_{cam} steradians and a resolution of I pixels, then the average pixel support is $\omega_{pix} = \frac{\omega_{cam}}{I}$. If the LIDAR laser’s beam divergence is ω_{laser} steradians, then the acuity increase from LIDAR to camera is $\frac{\omega_{laser}}{\omega_{pix}}$.

The goal of guided depth completion is to extract this potential increase in acuity by using large datasets to complete or upgrade the existing measurements. A flexible LIDAR can leverage such techniques by, for example, placing depth measurements in regions of interest.

Next, in Sect. 3.1, we discuss the MEMS-modulated transmitter optics that enable flexibility through fast, controlled scans. The cost, however, is that MEMS mirrors act as a small aperture that reduce signal-to-noise ratio (SNR). In the following Sect. 3.2 we model the receiver optical design space, comparing characteristics such as field-of-view (FOV), volume and signal-to-noise ratio (SNR).

3.1 MEMS Mirror based Transmitter Optics

The transmitter optics consist of the pulsed light source and MEMS mirror. The LIDAR's beam is steered by the mirror, whose azimuth and elevation are given by changes in control voltages over time, $(\theta(V(t)), \phi(V(t)))$ over the MEMS mirror FOV ω_{mirror} . The advantage of MEMS mirrors are compactness and speed, allowing the MEMS mirror scan to cover the FOV quickly, or attend to a region-of-interest given by an adaptive algorithm. The challenge in transmitter optics is to provide a powerful, narrow laser with low beam divergence, given by

$$\omega_{laser} \approx \frac{M^2 \lambda}{w_o \pi} \quad (1)$$

where M is a measure of laser beam quality and w_o refers to the radius at the beam waist, which we use a proxy for MEMS mirror size. Previous work has shown MEMS-mirror modulated LIDAR systems across this design space, ranging from high-quality lasers with Gaussian profiles, such as erbium fiber lasers used by [39], where M is near-unity, to low-cost edge-emitting diodes, such as [40] where $M \approx 300$ on the diode's major axis.

Our setup follows the low-cost diode route, but with an addition of a two-lens Keplerian telescope to reduce the beam waist to $6mm$ and an iris to match the MEMS mirror aperture. This is similar to the optical fiber used in [6].

3.2 Receiver Optics Design Tradeoffs

Design	Volume	FOV	SNR
Retroreflection	$\frac{\pi u w_o^2}{12}$	= MEMS FOV ω_{mirror}	$\frac{atan(\frac{w_o}{Z})}{\omega_{laser} Z tan(\frac{\omega_{laser}}{2})}$
Receiver array	$u A^2$	$\min(2 atan(\frac{A}{2u}), \omega_{mirror})$	$\frac{1}{2 Z tan(\frac{\omega_{laser}}{2})}$
Single detector . Conventional ($u \geq f$) Ours ($u < f$)	$\frac{\pi u A^2}{12}$	$\min(2atan(\frac{A(Z-f) \frac{Zu-fu-fZ}{Z-f} }{2u f Z}), \omega_{mirror})$	$\frac{1}{4Zatan(\frac{A(Z-f) \frac{Zu-fu-fZ}{Z-f} }{2u f Z})tan(\frac{\omega_{laser}}{2})}$

Table 2. RECEIVER MODELS.

From the previous section, we can denote the transmitter optics design space as a combination of laser quality M and MEMS mirror size w_o , which we write as $\Pi_t = \{M, w_o\}$. Now, we add receiver optics to the design space, which we denote as $\Pi_r = \{n, A, u, f\}$, where n^2 is the number of photodetectors in the receiver, A is the aperture, u is the distance between the photodetector array and the receiver optics and f is the focal length of the receiver optics. Therefore the full design space consists of both receiver/transmitter optics, $\Pi = \{\Pi_r, \Pi_t\}$.

We define the characterization of any instance within the design space Π as consisting of field-of-view Ω steradians, SNR s and volume V denoted as $\Xi = \{\Omega, s, V\}$. The range Z is determined by the SNR and the detector sensitivity. Computing these parameters depends on the design choices made, and we

provide simulations comparing diverse designs summarized in Fig. 3(I). These include retro-reflective receivers [14] (Fig. 3I(a)), receiver arrays [6] (Fig. 3I(b)) and single-pixel detectors [40] (Fig. 3I(c)).

Preliminaries: Full derivations for the three receiver designs, shown in Table 2, are in supplementary material. The table refers to receiver sensor volume, field-of-view and SNR. The *volume* is the convex hull of the opaque baffles that must contain the receiving transducer electronics and is either a cone or cuboid. The *FOV* is the range of angles that the receiver is sensitive to, and is obtained from the defocus kernel, upper-bounded by the MEMS FOV ω_{mirror} . For simplicity, trigonometric functions are written to act on steradian quantities, but in actuality act on the apex angle of the equivalent cone. Conventionally, *SNR* is the ratio of received laser intensity (i.e. signal power) to sensor noise. We use a definition closer to the area-solid angle product used in optics [30] for a canonical LIDAR transducer (with canonical noise), which can be loosely understand as loss of LIDAR laser dot intensity due to beam divergence and receiver aperture size.

Simulation-based comparisons to our proposed design: In our noiseless simulations, we assumed a geometric model of light. To illustrate the tradeoffs, we vary the laser quality between $M = 1$ to $M = 100$, representing an ideal Gaussian beam vs. a cheap laser diode. For the same reason, we vary the MEMS mirror size w_o from $0.1mm$ (10 times larger than the TI DMD [16]) to $5mm$ (a large size for a swiveling MEMS mirror). The range of dimensions over which we explore the receiver design space are of the order of a small camera, with apertures $0cm \leq A \leq 10cm$, focal lengths $0mm \leq f \leq 50mm$ and image plane-lens distances $0mm \leq u \leq 50mm$. In Fig. 3(II)-(IV) we describe our proposed, simple modification to the conventional single-pixel receiver, where photodetector is placed on the optical axis, at a distance v larger than the focal length f .

In the next few pages, we discuss simulations that compare our modification to retro-reflective receivers, receiver arrays and conventional single-pixel receivers. The **conclusion** from these simulations is that our design modification provides a new option for receiver design space tradeoffs. In contrast to existing work on defocusing received radiances for FOV adjustment and amplitude compensation (e.g. [30]), we do not require special optics (e.g. split lens) and we have large off-axis FOV since the MEMS is not the aperture for the receiver. This gives advantages when compared to alternate designs. For example, in volume, our design is smaller than receiver arrays but larger than retro-reflective designs. In contrast, for SNR, for low-cost laser diodes, this tradeoff reverses and our design has better SNR than retro-reflective designs but lower than arrays.

Retro-reflective receivers: If high-quality lasers, such as erbium fiber lasers [39] are used, where M is near-unity, then these can be coupled with a co-located receiver and a beamsplitter, as shown in Fig. 3I(a), where the detector lens distance is equal to the focal length $u = f$. From Table 2, we can see the ratio of retro-reflective volume to ours is $\frac{w_o}{A}$, which is usually less than one, since our designs have large apertures and MEMS mirrors are small. In other words,

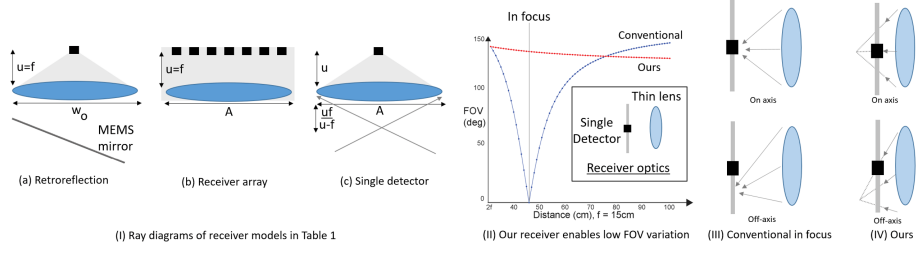


Fig. 3. OUR PROPOSED DESIGN VS. OTHER DESIGNS: In (I) we depict three common receiver designs: (a) retro-reflection, (b) receiver array and (c) single detectors. Our design is a variant of (c), where we suggest a simple optical trick, such that the single detector is placed within the focal distance of the lens. This enables consistent FOV over range, as shown by the red curve in (I) and in (III). Simulations for a $f = 15mm$ unit diameter lens.

retro-reflective designs are smaller than ours. The small retroreflective design also has the optimal FOV of the MEMS (due to co-location).

Our design does have an SNR advantage, because retroreflection requires the MEMS mirror to be the aperture for both receiver/transmitter. Consider a simplified SNR ratio from the table's last column, between retroreflection and

our sensor, given by $\frac{4Z \operatorname{atan}\left(\frac{A(Z-f)\|Zu-fu-fZ\|}{2ufZ}\right) \tan\left(\frac{\omega_{laser}}{2}\right) \operatorname{atan}\left(\frac{w_o}{2Z}\right)}{\omega_{laser} Z \tan\left(\frac{\omega_{laser}}{2}\right)}$, simplifying to

$$\frac{4 \operatorname{atan}\left(\frac{A(Z-f)\|Zu-fu-fZ\|}{2ufZ}\right) \operatorname{atan}\left(\frac{w_o}{2Z}\right)}{\omega_{laser}}. \text{ Assuming } Z \gg f, \text{ this gives } \frac{4 \operatorname{atan}\left(\frac{w_o}{2Z}\right) \operatorname{atan}\left(\frac{A(\|u-f\|)}{2uf}\right)}{\omega_{laser}}.$$

Plugging in the expression for the beam divergence ω_{laser} , we get

$$\frac{4w_o \pi \operatorname{atan}\left(\frac{w_o}{2Z}\right) \operatorname{atan}\left(\frac{A(\|u-f\|)}{2uf}\right)}{M^2 \lambda}. \text{ All the variables in this expression, except for } Z, \text{ are}$$

constant for a particular design. As the range increases and Z becomes large, this expression falls below 1, favoring our design. A high quality laser $M = 1$ or a large mirror size w_o can delay this eventuality, as shown in Fig. 4(Ia). For low-cost diodes, Fig. 4(Ib), we have higher SNR at close ranges too.

Receivers arrays: If cost and size are not issues, the receiver can be made large, such as a custom-built, large SPAD array [6] or a parabolic concentrator for 1.5mm detectors [39]. Comparing such arrays' volume, in Table 2's second column, we can easily see the cuboid-cone ratio of $\frac{12}{\pi}$ favors our design, and is unsurprisingly shown in Fig. 4(II) (left) across multiple focal lengths. On the other hand, it is clear that a large receiver array would have higher SNR. From the third column, assuming $Z \gg f$ and a similar argument to that previously done, the ratio between the receiver array and our design's SNR is $2 \operatorname{atan}\left(\frac{A(\|u-f\|)}{2uf}\right)$, which, for large aperture A , is always over 1 and is demonstrated in Fig. 4(II) (right) for the particular case of $M = 100, w_o = 5mm$, favoring our design. Even so arrays have larger SNR at all depths.

Single detector and proposed modification: Our approach is a single pixel receiver, which can allow for detection over a non-degenerate FOV if it is

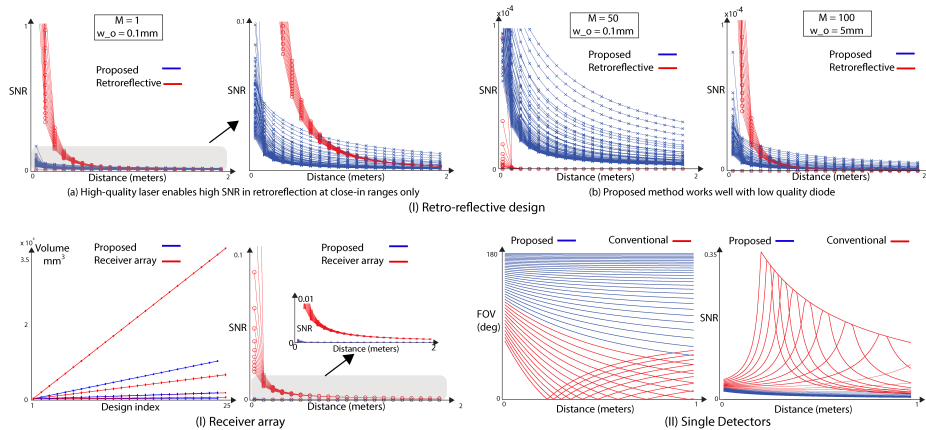


Fig. 4. NOISELESS SIMULATIONS COMPARING PROPOSED METHOD WITH RETRO-REFLECTIVE DESIGN, RECEIVER ARRAY AND CONVENTIONAL SINGLE DETECTORS: In (I) we compare the SNR of proposed method with retroreflection for different laser qualities and mirror sizes. A high-quality laser (I)(a) enables higher SNR for close-in scenes for retroreflective designs, but at large ranges, our method has higher SNR. In (II)(a) we show that our proposed design has lower volume than a receiver array, across a wide range of focal lengths, but a receiver array has a higher SNR (II)(b), even when compared to the best case for our sensor from (I). In (III) we compare our design with conventional single detectors, contrasting many sensor positions u for a lens with $f = 15\text{mm}$. Although our sensor shows consistent FOV ((III) left), it is always defocused, and faces an SNR cost ((III) right).

defocused, as shown for a scanning LIDAR by [40]. When the laser dot is out of focus, some part of it activates the single photodetector. If the laser dot is in focus, the activation area available is smaller, but more concentrated.

Our approach is based on a simple observation; placing the image plane between the lens and the focus, i.e. $v < f$, will guarantee that the laser dot will never be in focus. For imaging photographs, this is not desirable, but for detecting the LIDAR system's received pulse, amplitude is less important than timing information (i.e. pulse peak in our case). Further, this optical setup ensures that the angular extent of the dot is nearly constant over a large set of ranges. To see this, consider the second column of the table for our design. When $u < f$ and $z \gg f$, the FOV becomes $2\text{atan}(\frac{A(f-u)}{2uf})$. Suppose $u \ll f$, then we can rewrite as $2\text{atan}(\frac{A(1-\frac{u}{f})}{2u})$, which becomes $2\text{atan}(\frac{A}{2u})$, which is near-constant. This is supported by simulations (red curve) in Fig. 4(III) (left) and explained in the ray diagrams of Fig. 4(III) (right).

Of course, for the conventional approach, when $u = f$, there is a low FOV since the laser dot is sharply in focus. This is supported by simulations shown in Fig. 4(III), for $u > f$, shown in red, for settings of $f = 15\text{mm}$, $A = 100\text{mm}$, over a range of sensor sizes and ranges. Therefore, the FOV degenerates to a small value, where SNR is also the highest. Our design does not suffer this depth-

dependent FOV variation and is consistent across the range. However, as shown in the right of the figure, this results in a low SNR since the system is always defocused. In practice we find the consistent FOV to be more valuable than SNR, and, further, depth completion can improve raw measurements.

4 Enabling Real-time Adaptive Sampling

In contrast to other MEMS modulated LIDARs we do not run the MEMS mirror at resonance [11,39,22], but instead trace a specific scan pattern. The Mirrorcle mirror [29,28] that we use is capable of tens of KHz of scanning frequency for custom patterns, which is enough to sense most common dynamic objects.

Data	MRE (%)	RMSE (m)	\log_{10} (m)	δ_1 (%)	δ_2 (%)	δ_3 (%)
Real	10.16	.1659	.0410	89.80	95.88	98.63

Table 3. LIDAR EVALUATION: The table reports the mean relative error (MRE), root mean squared error (RMSE), average (\log_{10}) error and threshold accuracy (δ_i) of the calibrated depth measurements from our adaptive LIDAR prototype, relative to the “ground-truth” Kinect V2 depths, over 75 scenes from our Real dataset.

Many adaptive methods exist to find good scan patterns, represented as voltage-dependent mirror angles over time, $(\theta(V(t)), \phi(V(t)))$. These include open loop [4,10,40,6] real-time estimation of regions of interest (ROIs) as well as end-to-end learning to help decide where to sense next [24,3].

We term using such adaptive algorithms with our flexible platform as *foveating LIDAR*, since it increases resolution, similar to how our eyes’ fovea control which scene region is imaged in detail. **Our contribution** here is to demonstrate LIDAR foveation for dynamic scenes with an open-loop algorithm based on motion detection [10]. We now discuss the different experimental steps.

Experimental setup: Our LIDAR engine is a single beam Lightware SF30/C with an average power of $0.6mW$ and a pulse frequency of $36KHz$. This device is designed for outdoor use and can produce 1600 depth measurements per second at 100m. *Our focus is the MEMS-based foveating LIDAR* and a different LIDAR engine could provide more points or higher range or accuracy. Data is captured as a stream of depth measurements, and each are time-stamped by the MEMS direction, given by the voltage $V(t)$. We modulate the single beam with a $3.6mm$ Mirrorcle MEMS mirror. Our current prototype has a range of $3m$ (due to optical losses that can be optimized closer to the $100m$ max in newer versions) and a field-of-view of $\approx 25^\circ$. The laser dot, in steradians, is $6 \times 10^{-4}\Omega$ and this angular support is consistent over change in MEMS mirror angle.

Calibration and validation: Even with our novel optical system, the raw sensor measurements still provide depth discrimination. Since our sensor response is

linear, we apply a 1D calibration convert the LIDAR voltages into distances. We evaluate the quality of our sensor measurements and our calibration by computing the mean relative error (MRE), root mean squared error (RMSE), average (\log_{10}) error and threshold accuracy (δ_i) of the calibrated depth measurements from our LIDAR relative to the “ground-truth” Kinect V2 depths, over all 75 scenes of our real dataset, and these are reported in Table 3.



Fig. 5. ADAPTIVE LIDAR SAMPLING: A variety of sensing capabilities, such as foveating onto objects of interest and sub-sampling over the FOV for fast capture, are demonstrated. Each triplet consists of a color image of a scene captured by the co-located camera (top), the corresponding depth measurements captured by our LIDAR (middle), and the corresponding outputs from our deep depth completion network (bottom).

4.1 Depth completion

We now describe how to provide depth completion for the foveated but sparse measurements of our LIDAR. This builds on existing work [41,45] where the sparse depth measurements are captured by our flexible LIDAR sensor and the “guide” image is captured by a RGB camera that is co-located with the sensor. We train a DenseNet-inspired [17] encoder-decoder neural network to perform RGB-guided depth completion of sparse depth measurements.

Architecture. We adopt [1]’s encoder-decoder network architecture, except that our network has 4 input channels, as it expects inputs consisting of a sparse

depth map concatenated with an RGB image, whereas [1] only expects standard RGB images as inputs. The encoder component of our network is the same as DenseNet 169 minus the classification layer. The decoder component consists of a three convolutional blocks followed by a final 3×3 convolutional layer. Each bilinear upsampling block consists of two 3×3 convolutional layers (with a leaky ReLU), and 2×2 max-pooling.

Optimization. We adopt [1]’s loss as a weighted sum of three terms:

$$L(y, \hat{y}) = \lambda L_{depth}(y, \hat{y}) + L_{grad}(y, \hat{y}) + L_{SSIM}(y, \hat{y}) \quad (2)$$

where y and \hat{y} denote the ground-truth and estimated depth maps respectively, and λ denotes a weighting parameter, which we set to 0.1. The remaining terms are defined as in [1] which has full expressions for the losses.

Datasets and implementation details: We perform our evaluations using two datasets: a real dataset captured with our LIDAR system and a simulated Flexible LIDAR dataset generated by sub-sampling the NYUv2 Depth dataset [31]. The real dataset consists of pairs of RGB images and sparse depth measurements of 75 different scenes captured with our LIDAR system. For each of the 75 scenes, we also capture a dense “ground-truth” depth map using a Kinect V2 depth sensor that is stereo calibrated with our LIDAR system. All real dataset images are used exclusively for testing. The simulated dataset is split into non-overlapping train, test, and validation scenes.

Data	Method	MRE (%)	RMSE (m)	\log_{10} (m)	δ_1 (%)	δ_2 (%)	δ_3 (%)
NYU	Mono	8.55	.3800	.0361	90.56	98.08	98.56
	Ours	5.89	.2488	.0245	97.69	99.68	99.92
Real	Mono	28.26	.3711	.1090	50.14	87.38	96.00
	Ours	12.29	.1668	.0395	85.86	95.89	99.18

Table 4. BASE COMPARISON TO MONOCULAR DEPTH ESTIMATION: As a baseline, we compare the dense depth maps generated by our guided depth completion network to state-of-the-art monocular depth estimation [1]. We perform this evaluation for a sub-sampled version of the NYUv2 Depth [31] dataset and a real dataset captured with our adaptive LIDAR prototype. All results are at 30fps.

We train the model described in section 4.1 on a simulated Flexible LIDAR dataset generated by sub-sampling the NYUv2 Depth dataset. During training, depths were randomly scaled to prevent the network from overfitting to the color camera used to capture the RGB images in the NYUv2 dataset. For optimization, we used Adam [21] with $\beta_1 = 0.9$, $\beta_2 = 0.999$, $\epsilon = 1e-8$ and a learning rate of 0.0001, and a batch size of 4. The learning rate was dropped to 0.00001 after 94k iterations. We used Xavier initialization for the first layer of our network. All other layers were initialized with the pre-trained weights from [1] for monocular

Data	FPS	MRE (%)	RMSE (m)	\log_{10} (m)	δ_1 (%)	δ_2 (%)	δ_3 (%)
NYU	30	5.89	.2488	.0245	97.69	99.68	99.92
	24	5.88	.2430	.0244	97.97	99.70	99.92
	18	5.59	.2261	.0233	98.50	99.77	99.94
	12	5.65	.2255	.0236	98.52	99.77	99.94
	6	5.15	.1879	.0217	99.32	99.91	99.98
Real	30	12.29	.1668	.0395	85.86	95.89	99.18
	24	12.09	.1644	.0446	86.34	96.04	99.26
	18	11.57	.1578	.0430	87.27	96.61	99.30
	12	11.59	.1558	.0435	88.26	97.01	99.33
	6	11.19	.1537	.0422	88.10	97.19	99.26

Table 5. EVALUATION OF GUIDED DEPTH COMPLETION. We demonstrate the flexibility and robustness of our Adaptive LIDAR framework by evaluating the dense depth maps generated by our guided depth completion network across a range of frame rates (FPS) and two datasets: a sub-sampled version of NYUv2 Depth [31] and a Real dataset captured with our adaptive LIDAR. Errors are computed relative to depth maps captured by a Microsoft Kinect V1 for NYUv2 and Kinect V2 for the Real dataset.

Data	FPS	Method	MRE (%)	RMSE (m)	\log_{10} (m)	δ_1 (%)	δ_2 (%)	δ_3 (%)
NYU	30	Full FOV	5.52	.2392	.0231	98.24	99.86	99.98
		Foveated	4.81	.1845	.0202	99.50	99.97	100.0
Real	30	Full FOV	15.72	.1925	.0566	80.30	93.79	99.36
		Foveated	13.36	.1589	.0497	83.24	97.80	99.46

Table 6. DEPTH COMPLETION ON FOVEATED LIDAR DATA: We leverage foveation to improve the quality of the dense depth maps generated by our depth completion network, in regions of interest, while maintaining the same LIDAR frame rate (FPS). We report these results for a sub-sampled version of the NYUv2 Depth [31] dataset and a real dataset captured with our adaptive LIDAR Prototype. Errors are computed only in regions of interest.

depth estimation on NYUv2. We adopt a number of data augmentation strategies, such as random resizing the input images such that the small dimension was of size 640, 832, or 1024 and then were randomly cropped to resized inputs of 640×480 . Additionally, the RGB channels were randomly shuffled.

Basic validation against monocular depth estimation: As a minimum baseline, we compare the dense depth maps generated by our guided depth completion network to depth maps generated by a state-of-the-art monocular depth estimation network [1] in Table 4. Across all six error metrics and both datasets, guided depth completion far outperforms monocular depth estimation.

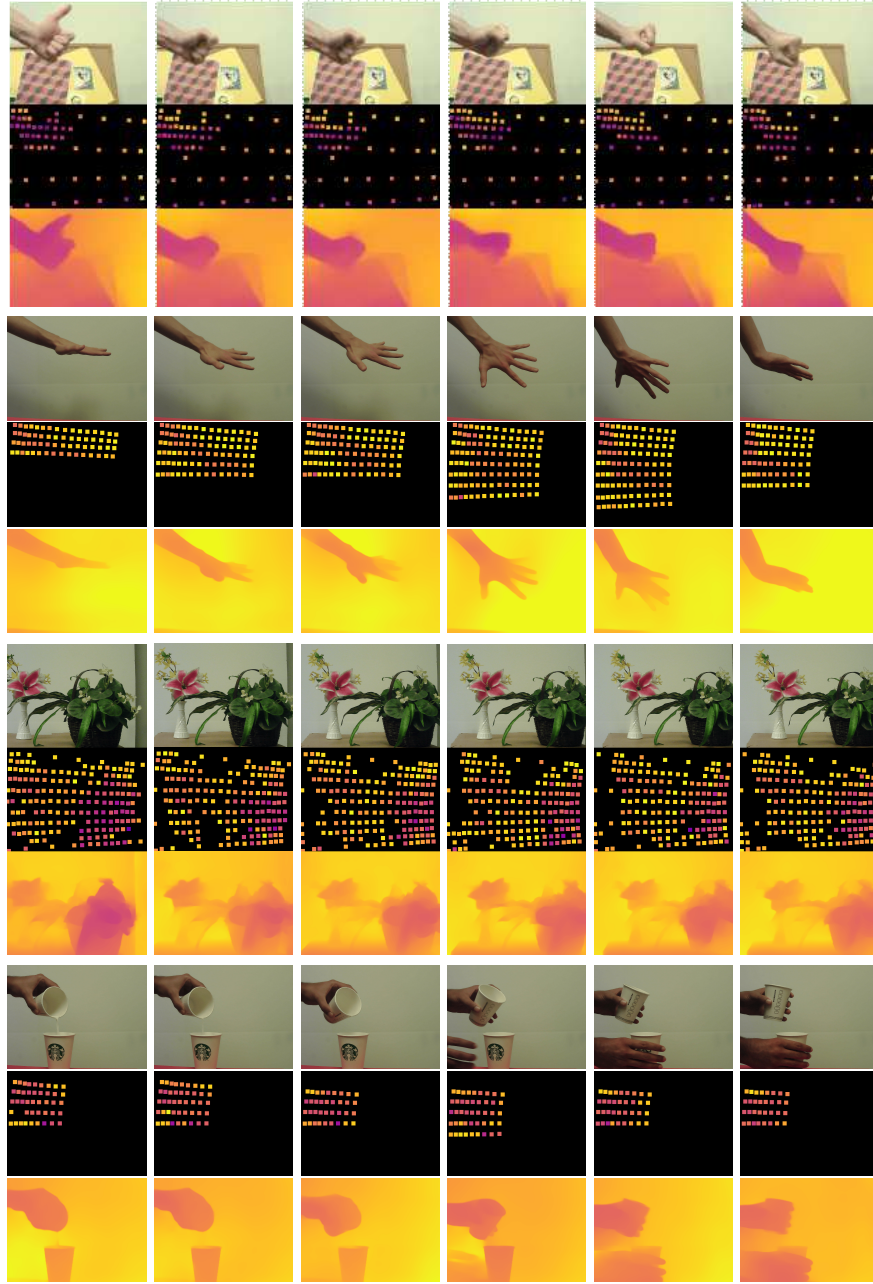


Fig. 6. MOTION-BASED ADAPTIVE SENSING: As the object moves, we use background subtraction to detect the region of interest and the MEMS-modulated LIDAR puts the samples where the object is located. Each triplet consists of a color image of the scene captured by the color camera co-located with our LIDAR (top), the corresponding depth measurements captured by our LIDAR (middle), and the corresponding outputs from our deep depth completion network (bottom).

4.2 Motion-based Foveated Depth Sampling

Our flexible platform allows us to ask if foveated LIDAR sampling improves depth measurements. We evaluate the performance of our guided depth completion network on LIDAR data captured with two different sampling regimes, full field-of-view sampling and foveated sampling in regions of interest, at various frame rates. Table 5 shows our evaluation for full field-of-view sampling. Table 6 demonstrates that foveation improves reconstruction in a region of interest, with qualitative results in Figures 5 and 6.

We also perform foveated sampling in real-time, using an open-loop motion-based system to determine the scan patterns. For a dynamic scene, a foveating LIDAR can have fewer samples in the right places, decreasing latency and improving frame-rate. In Fig. 6, we show objects moving across the scene. At each instance, the system performs background subtraction to segment a motion mask. This mask drives the LIDAR sampling, which has less points than a full dense scan would have, and therefore has higher sampling rate. Note that as the object changes position, the ROI changes and the LIDAR senses a different area. If temporal sampling is not the focus, then the method can instead densely sample the points onto the region of interest, increasing the angular resolution (i.e. zooming). Finally, we note that all results include depth completion of the measurements, showing that high-quality results can be obtained.

5 Limitations and Conclusions

Our LIDAR engine has a 100m range and is designed for outdoor use, but unnecessary optical losses reduce this to around 3m. For future prototypes we wish to remove these losses with a GRIN lens, as done by [11]. In conclusion, our prototype enables the kind of flexibility that have so far only been seen in simulated experiments and follows a recent trend in computational photography to use data-driven approaches inside the sensor [5,8,7,38].

Acknowledgements

The University of Florida authors have been partially supported by the National Science Foundation through NSF IIS: 1909729, and the Office of Naval Research through ONR N00014-18-1-2663.

References

1. Alhashim, I., Wonka, P.: High quality monocular depth estimation via transfer learning. arXiv preprint arXiv:1812.11941 (2018)
2. Bartels, J.R., Wang, J., Whittaker, W., Narasimhan, S.G.: Agile depth sensing using triangulation light curtains. In: Proceedings of the IEEE International Conference on Computer Vision. pp. 7900–7908 (2019)

3. Bergman, A., Lindell, D., Wetzstein, G.: Deep adaptive lidar: End-to-end optimization of sampling and depth completion at low sampling rates. ICCP (2020)
4. Breivik, G.M., Thielemann, J.T., Berge, A., Skotheim, Ø., Kirkhus, T.: A motion based real-time foveation control loop for rapid and relevant 3d laser scanning. In: CVPR 2011 WORKSHOPS. pp. 28–35. IEEE (2011)
5. Chakrabarti, A.: Learning sensor multiplexing design through back-propagation. In: Advances in Neural Information Processing Systems. pp. 3081–3089 (2016)
6. Chan, S., Halimi, A., Zhu, F., Gyongy, I., Henderson, R.K., Bowman, R., McLaughlin, S., Buller, G.S., Leach, J.: Long-range depth imaging using a single-photon detector array and non-local data fusion. Scientific reports **9**(1), 8075 (2019)
7. Chang, J., Sitzmann, V., Dun, X., Heidrich, W., Wetzstein, G.: Hybrid optical-electronic convolutional neural networks with optimized diffractive optics for image classification. Scientific reports **8**(1), 12324 (2018)
8. Chen, H.G., Jayasuriya, S., Yang, J., Stephen, J., Sivaramakrishnan, S., Veer-araghavan, A., Molnar, A.: Asp vision: Optically computing the first layer of convolutional neural networks using angle sensitive pixels. In: Proceedings of the IEEE Conference on Computer Vision and Pattern Recognition. pp. 903–912 (2016)
9. Chen, Z., Badrinarayanan, V., Drozdov, G., Rabinovich, A.: Estimating depth from rgb and sparse sensing. In: Proceedings of the European Conference on Computer Vision (ECCV). pp. 167–182 (2018)
10. Ferrari, S.: Track coverage in sensor networks. In: 2006 American Control Conference. pp. 7–pp. IEEE (2006)
11. Flatley, T.P.: Spacecube: A family of reconfigurable hybrid on-board science data processors (2015)
12. Gruber, T., Julca-Aguilar, F., Bijelic, M., Ritter, W., Dietmayer, K., Heide, F.: Gated2depth: Real-time dense lidar from gated images. arXiv preprint arXiv:1902.04997 (2019)
13. Hall, D.S.: High definition lidar system (Jun 28 2011), uS Patent 7,969,558
14. Halterman, R., Bruch, M.: Velodyne hdl-64e lidar for unmanned surface vehicle obstacle detection. Tech. rep., SPACE AND NAVAL WARFARE SYSTEMS CENTER SAN DIEGO CA (2010)
15. Hawkins, T., Einarsson, P., Debevec, P.E.: A dual light stage. Rendering Techniques **5**, 91–98 (2005)
16. Hornbeck, L.J.: Architecture and process for integrating dmd with control circuit substrates (May 28 1991), uS Patent 5,018,256
17. Huang, G., Liu, Z., Van Der Maaten, L., Weinberger, K.Q.: Densely connected convolutional networks. In: Proceedings of the IEEE conference on computer vision and pattern recognition. pp. 4700–4708 (2017)
18. Hui, T.W., Loy, C.C., Tang, X.: Depth map super-resolution by deep multi-scale guidance. In: Proceedings of European Conference on Computer Vision (ECCV) (2016)
19. Jones, A., McDowall, I., Yamada, H., Bolas, M., Debevec, P.: Rendering for an interactive 360 light field display. ACM Transactions on Graphics (TOG) **26**(3), 40 (2007)
20. Kasturi, A., Milanovic, V., Atwood, B.H., Yang, J.: Uav-borne lidar with mems mirror-based scanning capability. In: Proc. SPIE. vol. 9832, p. 98320M (2016)
21. Kingma, D.P., Ba, J.: Adam: A method for stochastic optimization. arXiv preprint arXiv:1412.6980 (2014)
22. Krastev, K.T., Van Lierop, H.W., Soemers, H.M., Sanders, R.H.M., Nellissen, A.J.M.: Mems scanning micromirror (Sep 3 2013), uS Patent 8,526,089

23. Lindell, D.B., O’Toole, M., Wetzstein, G.: Single-photon 3d imaging with deep sensor fusion. *ACM Transactions on Graphics (TOG)* **37**(4), 113 (2018)
24. Liu, C., Gu, J., Kim, K., Narasimhan, S., Kautz, J.: Neural rgb-to-d sensing: Depth and uncertainty from a video camera. arXiv preprint arXiv:1901.02571 (2019)
25. Lu, J., Forsyth, D.: Sparse depth super resolution. In: *Proceedings of the IEEE Conference on Computer Vision and Pattern Recognition*. pp. 2245–2253 (2015)
26. Lucas, B.D., Kanade, T., et al.: An iterative image registration technique with an application to stereo vision (1981)
27. Mal, F., Karaman, S.: Sparse-to-dense: Depth prediction from sparse depth samples and a single image. In: *2018 IEEE International Conference on Robotics and Automation (ICRA)*. pp. 1–8. IEEE (2018)
28. Milanović, V., Kasturi, A., Siu, N., Radojčić, M., Su, Y.: memseye for optical 3d tracking and imaging applications. In: *Solid-State Sensors, Actuators and Microsystems Conference (TRANSDUCERS), 2011 16th International*. pp. 1895–1898. IEEE (2011)
29. Milanović, V., Kasturi, A., Yang, J., Hu, F.: A fast single-pixel laser imager for vr/ar headset tracking. In: *Proc. of SPIE Vol. vol. 10116*, pp. 101160E–1 (2017)
30. Mudge, J.: Range-compensating lens for non-imaging active optical systems. *Applied optics* **58**(28), 7921–7928 (2019)
31. Nathan Silberman, Derek Hoiem, P.K., Fergus, R.: Indoor segmentation and support inference from rgb-d images. In: *ECCV* (2012)
32. Nayar, S.K., Branzoi, V., Boult, T.E.: Programmable imaging using a digital micromirror array. In: *Proceedings of the 2004 IEEE Computer Society Conference on Computer Vision and Pattern Recognition, 2004. CVPR 2004. vol. 1*, pp. I–I. IEEE (2004)
33. Newcombe, R.A., Izadi, S., Hilliges, O., Molyneaux, D., Kim, D., Davison, A.J., Kohi, P., Shotton, J., Hodges, S., Fitzgibbon, A.: Kinectfusion: Real-time dense surface mapping and tracking. In: *2011 10th IEEE International Symposium on Mixed and Augmented Reality*. pp. 127–136. IEEE (2011)
34. O’Toole, M., Lindell, D.B., Wetzstein, G.: Confocal non-line-of-sight imaging based on the light-cone transform. *Nature* **555**(7696), 338 (2018)
35. Raskar, R., Welch, G., Cutts, M., Lake, A., Stessin, L., Fuchs, H.: The office of the future: A unified approach to image-based modeling and spatially immersive displays. In: *Proceedings of the 25th annual conference on Computer graphics and interactive techniques*. pp. 179–188. ACM (1998)
36. Riegler, G., Rüther, M., Bischof, H.: Atgv-net: Accurate depth super-resolution. In: *European Conference on Computer Vision*. pp. 268–284. Springer (2016)
37. Sandner, T., Baulig, C., Grasshoff, T., Wildenhain, M., Schwarzenberg, M., Dahlmann, H.G., Schwarzer, S.: Hybrid assembled micro scanner array with large aperture and their system integration for a 3d tof laser camera. In: *MOEMS and Miniaturized Systems XIV. vol. 9375*, p. 937505. International Society for Optics and Photonics (2015)
38. Sitzmann, V., Diamond, S., Peng, Y., Dun, X., Boyd, S., Heidrich, W., Heide, F., Wetzstein, G.: End-to-end optimization of optics and image processing for achromatic extended depth of field and super-resolution imaging. *ACM Transactions on Graphics (TOG)* **37**(4), 114 (2018)
39. Stann, B.L., Dammann, J.F., Del Giorno, M., DiBerardino, C., Giza, M.M., Powers, M.A., Uzunovic, N.: Integration and demonstration of mems-scanned lidar for robotic navigation. In: *Proc. SPIE. vol. 9084*, p. 90840J (2014)
40. Tasneem, Z., Wang, D., Xie, H., Koppal, S.J.: Directionally controlled time-of-flight ranging for mobile sensing platforms. In: *Robotics: Science and Systems* (2018)

41. Uhrig, J., Schneider, N., Schneider, L., Franke, U., Brox, T., Geiger, A.: Sparsity invariant cnns. In: 2017 International Conference on 3D Vision (3DV). pp. 11–20. IEEE (2017)
42. Van Gansbeke, W., Neven, D., De Brabandere, B., Van Gool, L.: Sparse and noisy lidar completion with rgb guidance and uncertainty. arXiv preprint arXiv:1902.05356 (2019)
43. Wang, J., Bartels, J., Whittaker, W., Sankaranarayanan, A.C., Narasimhan, S.G.: Programmable triangulation light curtains. In: Proceedings of the European Conference on Computer Vision (ECCV). pp. 19–34 (2018)
44. Yamamoto, T., Kawanishi, Y., Ide, I., Murase, H., Shinmura, F., Deguchi, D.: Efficient pedestrian scanning by active scan lidar. In: Advanced Image Technology (IWAIT), 2018 International Workshop on. pp. 1–4. IEEE (2018)
45. Zhang, Y., Funkhouser, T.: Deep depth completion of a single rgb-d image. In: Proceedings of the IEEE Conference on Computer Vision and Pattern Recognition. pp. 175–185 (2018)

Supplementary Material: A MEMS-based Foveating LIDAR to enable Real-time Adaptive Depth Sensing

Francesco Pittaluga ^{*1} Zaid Tasneem ^{*3} Justin Folden ^{*3}
Brevin Tilmon ³ Ayan Chakrabarti ² Sanjeev J. Koppal ³

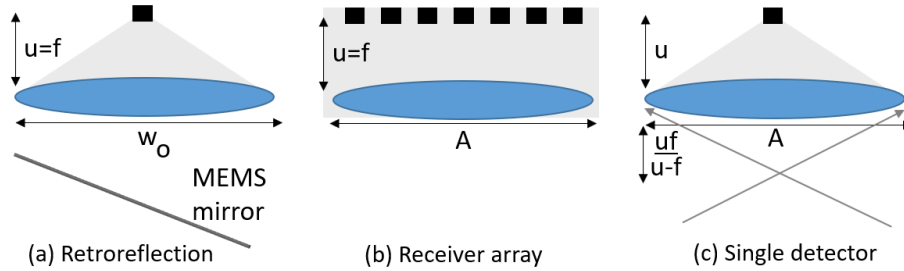
¹ NEC Labs America ² Washington University in St. Louis
³ University of Florida

1 Derivations

Design	Volume	FOV	SNR
Retroreflection	$\frac{\pi u w_0^2}{12}$	= MEMS FOV ω_{mirror}	$\frac{atan(\frac{w_0}{2Z})}{\omega_{laser} Z tan(\frac{\omega_{laser}}{2})}$
Receiver array	$u A^2$	$\min(2 atan(\frac{A}{2u}), \omega_{mirror})$	$\frac{1}{2 Z tan(\frac{\omega_{laser}}{2})}$
Single detector <i>Conventional</i> ($u \geq f$) <i>Ours</i> ($u < f$)	$\frac{\pi u A^2}{12}$	$\min(2atan(\frac{A(Z-f) \parallel \frac{Zu-fu-fZ}{Z-f} \parallel}{2ufZ}), \omega_{mirror})$	$\frac{1}{4Zatan(\frac{A(Z-f) \parallel \frac{Zu-fu-fZ}{Z-f} \parallel}{2ufZ})tan(\frac{\omega_{laser}}{2})}$

Table 1. RECEIVER MODELS.

Here we derive all the formulae in Table 1 for the three designs. We have provided the ray diagrams of the designs in Fig. 1 and we have reproduced Table 1 here.



(I) Ray diagrams of receiver models in Table 1

Fig. 1. RAY DIAGRAMS OF DESIGNS.

^{*} Equal Contribution

1.1 Volume

For the retroreflection and single detector, the volume of the camera is a cone whose vertex is the location of the single detector. From the ray diagrams and from the equation of the volume of a cone, this is easily seen to be $\frac{\pi u w^2}{12}$ for the retroreflector and $\frac{\pi u A^2}{12}$ for the single detector. For the receiver array the volume is the entire enclosure, given by the volume of a cuboid, $u * A * A$.

1.2 FOV

The retroreceiver has exactly the FOV of the mirror, by definition. From 1(b), the FOV of the receiver array is given by the vertex angle of the cone at the central pixel, given by $2atan(\frac{A}{2u})$, bounded by the FOV of the mirror. This assumes the receiver and transmitter are close enough to ignore angular overlap issues.

To find the FOV of the single detector, consider the diagram in Fig. 3, where the single detector is focused on the laser dot at distance Z from the sensor. From similar triangles, the kernel size is given by first finding the in-focus plane at u' from the lens equation

$$\frac{1}{f} = \frac{1}{u'} + \frac{1}{Z} \quad (1)$$

and so $u' = \frac{fZ}{(Z-f)}$. From the two vertex shared similar triangles on the left of the lens, we now have an expression for the kernel size

$$kernsize = abs(u - u') * \frac{A}{u} \quad (2)$$

Substituting the value of u' , we get an expression for $kernsize =$

$$abs(u - \frac{fZ}{(Z-f)}) * \frac{A}{\frac{fZ}{(Z-f)}} = \frac{A(Z-f)\|(Zu-fu-fZ)\|}{fZ\|Z-f\|} = \frac{A(Z-f)\|\frac{Zu-fu-fZ}{Z-f}\|}{fZ} \quad (3)$$

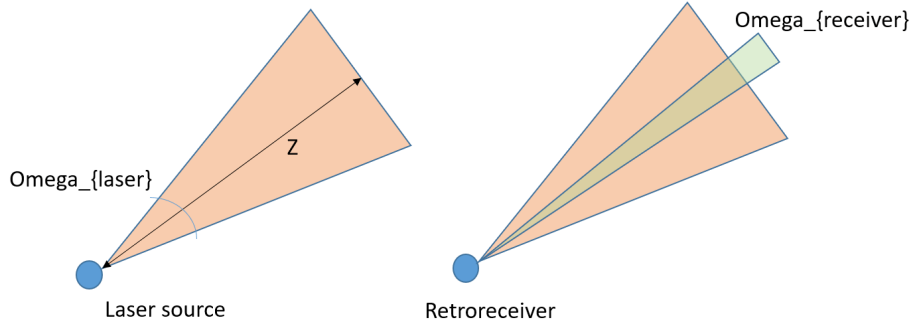
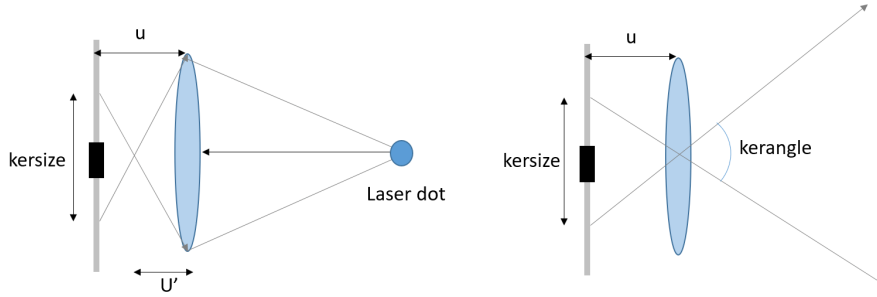
From the figure, the FOV, given by kernelangle is

$$2atan(\frac{kernsize}{2u}) = 2atan(\frac{A(Z-f)\|\frac{Zu-fu-fZ}{Z-f}\|}{2ufZ}) \quad (4)$$

1.3 SNR

From Fig. 2, the power from the laser decreases with distance. This is just fall-off from the source, and we represent it here as the area of the laser dot on a fronto-parallel plane. From the figure, this can be calculated from simple trigonometry as $2Ztan(\frac{\omega_{laser}}{2})$, and we use the reciprocal for the SNR as $\frac{1}{2Ztan(\frac{\omega_{laser}}{2})}$.

1. Receiver array: The receiver array is assumed to capture all the available radiance from the laser dot, and so the SNR is exactly the same as the power


Fig. 2. RETROREFLECTIVE SNR.

Fig. 3. SINGLE DETECTOR SNR.

fall-off described above as $\frac{1}{2Z \tan(\frac{\omega_{laser}}{2})}$.

2. Retroreflection: As can be seen in the right of Fig. 2, the ratio of the received angle to the transmitted angle gives the fraction of the received radiance from the laser dot. From Fig. 1(a), the single detector receives parallel light of width w_o . For any particular depth Z therefore, the angle subtended by this width at the sensor decreases and is given by $\omega_{receiver} = 2 \operatorname{atan}(\frac{w_o}{2Z})$ and the fraction of the fall-off received is given by $\frac{2 \operatorname{atan}(\frac{w_o}{2Z})}{\omega_{laser}}$. Multiplying this with the fall-off above gives $\frac{2 \operatorname{atan}(\frac{w_o}{2Z})}{\omega_{laser}} * \frac{1}{2Z \tan(\frac{\omega_{laser}}{2})} = \frac{\operatorname{atan}(\frac{w_o}{2Z})}{\omega_{laser} Z \tan(\frac{\omega_{laser}}{2})}$. Note this assumes that $\omega_{receiver} < \omega_{laser}$, and if this is not the case then a max function must be added so that $\omega_{receiver}$ does not exceed ω_{laser} .

3. Single detector: We just reduce the fall-off by the kerangle calculated before, and therefore the SNR is $\frac{1}{\kerangle * 2Z \tan(\frac{\omega_{laser}}{2})} = \frac{1}{4Z \operatorname{atan}(\frac{A(Z-f) \parallel \frac{Zu-fu-fZ}{Z-f} \parallel}{2uf}) \tan(\frac{\omega_{laser}}{2})}$